IET Science, Measurement & Technology

Research Article

IET Journals
The Institution of Engineering and Technology

Enhancement method of magnetic flux leakage signals for rail track surface defect detection

ISSN 1751-8822
Received on 30th November 2018
Revised 12th January 2020
Accepted on 28th February 2020
E-First on 29th April 2020
doi: 10.1049/iet-smt.2018.5651
www.ietdl.org

Yinliang Jia[1], Kangwu Liang[1] ✉, Ping Wang[1], Kailun Ji[1], Peng Xu[1]

[1]College of Automation Engineering, Nanjing University of Aeronautics and Astronautics, Nanjing 211106, People's Republic of China
✉ *E-mail: 406770928@qq.com*

Abstract: Magnetic flux leakage (MFL) detection is widely used for non-destructive testing of rails, pipelines and storage tanks. The leakage magnetic field (LMF) of a defect, especially a small defect, is usually weak. To find small defects on the rail surface, here a ferrite is added in an LMF sensor to reduce the reluctance to increase the magnetic intensity above the defects. The effects of the cross-sectional shape and size of a ferrite are studied by simulation and experiments, and the suitable dimensions for signal enhancement are found. To suppress the interference caused by the variation of the lift-off distance, two Hall sensors are introduced and a differential circuit is designed for signal post-processing. From the finite element simulation and experiments, it is shown that the MFL signals with a ferrite are significantly increased.

1 Introduction

The structural performance and service status of rails are of great importance to the safety of railway transportation. Therefore, a variety of non-destructive testing methods are used for defect detection [1, 2], such as the commonly used ultrasonics and eddy current techniques. However, the ultrasonic method cannot detect the fatigue damage on the surface of the rail [3–5]. Moreover, the eddy current approach is not suitable for quick detection [6, 7].

Magnetic flux leakage (MFL) detection can be used to find defects in the surface of rails, pipes and tanks [8–11]. Research has been done to improve the performance sensitivity of the MFL detection. Wu *et al.* [12] used a ferromagnetic support in a pipeline MFL detection system. Okolo and Meydan [13] proposed a quantitative approach based on impulse excitation to inspect far-surface hairline cracks.

The MFL signal of a defect is usually weak and difficult to detect. Various probe structures have been designed to solve this problem. For example, to detect tiny defects in bearing rings, a magnetic core with an open gap can be employed to guide the leaked magnetic flux into a magnetic circuit, where an induction coil is placed to sense the change of the magnetic flux [14]. Tsukada *et al.* [15] proposed unsaturated AC MFL testing with a magnetic resistance gradiometer to increase the MFL signal, and the defects in steels were successfully found. Wu *et al.* [16] developed a composite MFL method using alternating magnetic-field excitation in the pipeline inspection. However, the method requires complicated signal generation circuit and demodulating circuits, which may cause interferences and require high-frequency excitation for detection at a high speed.

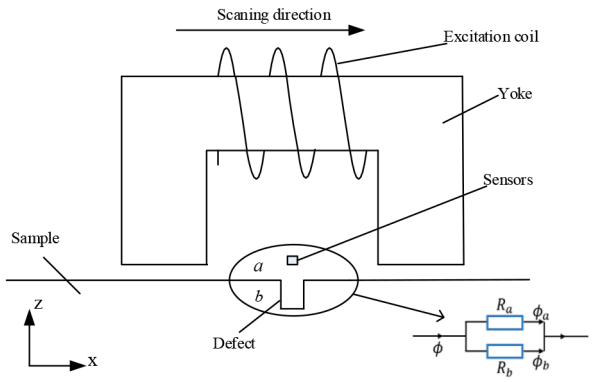

Fig. 1 *Conventional MFL model*

The density distribution of MFL is different at different lift-off distances [17, 18]. Usually, the smaller the lift-off is, the larger the MFL signal is. Li *et al.* [19] proposed a micro-magnetic bridge method, which consisted of a micro-magnetic bridge probe with high spatial resolution and an induction coil. Small defects were found at a small lift-off distance.

In real scenarios, the lift-off distance is usually large. For example, if the relative motion speed between the sensor and object measured is high, the lift-off should be large enough to prevent any unwanted collisions. However, in that case, the signal received is small and small defects may not be detected. If the detector has violent vibrations, the lift-off always changes and accordingly the output fluctuates. This will cause interference to defect detection. Bai *et al.* [20] reduced this interference by filtering with a rail surface adaptive and bearing mechanism.

It is concluded that MFL signal enhancement is necessary for detection of small defects when the lift-off is large. An appropriate probe structure is needed to improve the measurement sensitivity and reduce the interference caused by the lift-off variations.

In this work, the distribution of leakage magnetic field (LMF) on the surface of ferromagnetic materials is studied, and then a new method to enhance the MFL signals of rail track surface defects is proposed.

2 Theoretical analysis of the MFL

An MFL detector and the two-dimensional coordinate system used are illustrated in Fig. 1. The yoke and Hall sensor move along the *X*-axis above the surface of a ferromagnetic sample. Around a defect, the magnetic field is unevenly distributed. Some magnetic-field lines bend and leak into the air outside the sample [21, 22]. The sensor detects the LMF to find the defect.

The closed magnetic circuit satisfies the Ampere's law

$$\mathrm{NI} = \sum_i H_i l_i = \sum_i \frac{B_i l_i}{\mu_i} = \sum_i \frac{\Phi_i l_i}{\mu_i S_i} \tag{1}$$

where N is the number of turns of the yoke excitation coil. I is the current. NI is the electromotive force. H_i, B_i, Φ_i, μ_i, S_i and l_i are the magnetic-field intensity, magnetic flux density, magnetic flux, magnetic permeability, cross-sectional area and length of the ith

magnetic path, respectively. The magnetic fluxes of these sections Φ_i in the closed magnetic circuit are equal. So (2) can be written as

$$\mathrm{NI} = \Phi \sum_i \frac{l_i}{\mu_i S_i} = \Phi \sum_i R_i \tag{2}$$

where $l_i/\mu_i S_i$ is the magnetic reluctance of the ith magnetic circuit and can be expressed by R_i. The magnetic circuit for MFL detection can be divided into a yoke, two air gaps and a portion of the sample.

The magnetic circuits around the defect are simplified as shown in Fig. 1. The magnetic field is divided into two parts, that is, a and b. The magnetomotive force near the defect is F, which can be given by

$$F = \Phi_a R_a = \Phi_b R_b \tag{3}$$

$$\Phi = \Phi_a + \Phi_b \tag{4}$$

Furthermore

$$\Phi_a = \frac{\Phi R_b}{R_a + R_b} \tag{5}$$

Since the magnetic permeability of the sample and yoke is much larger than that of air, the reluctance of the magnetic circuit b is much larger than that of the magnetic circuit a. Φ is mainly determined by magnetic circuit b and basically unchanged when a ferrite is placed in the magnetic circuit a. It is also assumed that the air gap length and cross-sectional area of the magnetic circuit remain the same and the eddy current effect is not considered. Therefore, if a ferrite is placed in the magnetic circuit a, R_a will be reduced as the magnetic permeability of the ferrite is much larger than that of air. This ferrite is called a ferrite magnetism gatherer (FMG). Φ and R_b are not changed, so Φ_a will be increased according to (5), which means the MFL signal is enhanced.

3 Simulation results and analysis

Both magnetostatic and transient simulations are performed separately using ANSYS Maxwell software. The properties of the probe, sample and defect are listed in Table 1. The effects of different shapes and sizes of the FMG and the capability of magnetism gathering are studied.

3.1 Influence on the distribution of magnetic field

Static simulation is done with a conventional MFL model and the proposed model with FMGs in various sizes and shapes. The distribution of magnetic fields near a defect without an FMG is shown in Fig. 2. The magnetic flux density inside the defect is strong, while the LMF intensity is weak. An FMG is added to a position 3 mm above the defect. The static magnetic-field simulation results are shown in Fig. 3. Four cross-sectional shapes are analysed, i.e. round, square, rectangle and diamond. Compared to the case with no FMG, the magnetic flux density inside the defect is reduced, and the electromagnetic field outside the defect is varied. Under the FMG, the magnetic flux density is low.

Comparing these four shapes, the magnetic-field distribution in Fig. 3*a* is found special. The internal magnetic flux density is even, and the magnetic-field lines are not aggregated. A large magnetic flux concentration area is on each side of the FMG, but the magnetic flux density is weak. These are different from the other setups.

The magnetic-field distributions in Figs. 3*b* and *d* are similar. Owing to the parallel surface, the magnetic-field lines aggregate at the upper and lower edges, which is due to the shape anisotropy. The magnetic-field lines are dense on the upper and lower surfaces of the cross-sections, and the magnetic flux density of the lower surface is stronger. In addition, there are magnetic flux density converging areas at four right angles, and the flux density is strong inside the FMG. A magnetic accumulation area is outside the FMG. The magnetic flux density inside the rectangular FMG is stronger. It is indicated that the FMG with a rectangular cross-section has better magnetic focusing capabilities.

For the diamond cross-section, due to the fact that no edge is parallel to the upper surface of the sample, no significant magnetic gathering area is found at the edges in Fig. 3*c*. The magnetic flux density is large at the right and left angles, while the density is weak at the upper and lower angles.

The effect of the FMG with a circular or diamond cross-section is poor. Hence, a rectangular or square shape should be adopted. For the following study of the effect of the FMG size, the square one is analysed.

The relationship between the maximum magnetic flux density and side length of a square cross-section is shown in Fig. 4. Taking into account the simulation calculation error, a quadratic polynomial curve is generated to fit data. The magnetic flux density near the FMG increases with increasing side length.

Table 1 Properties of the materials defined in the simulation

Part	Material	Relative permeability (μ_r)	Electrical conductivity (σ, S/m)
excitation coil	copper	1	5.8×10^7
yoke and FMG	ferrite	1000	0.01
sample	Steel_1008	*B–H* curve with μ_r in the range of 1–1200	2×10^6
defect	rectangular air slot	1	0

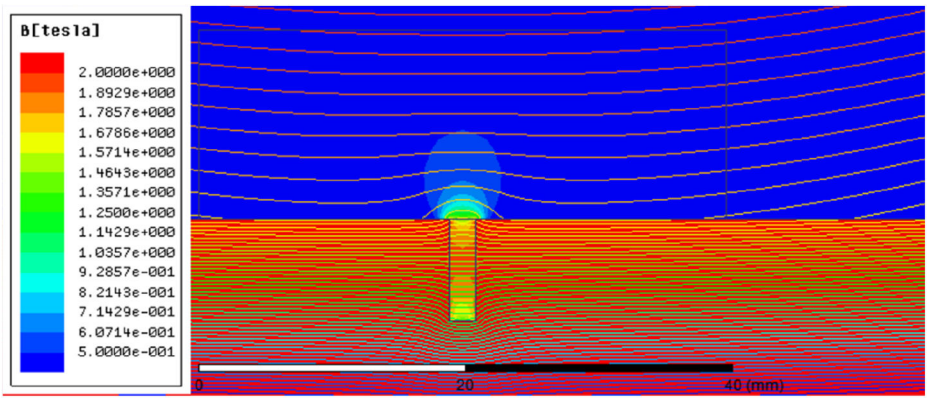

Fig. 2 *Distribution of the magnetic fields near a defect in the conventional MFL testing model*

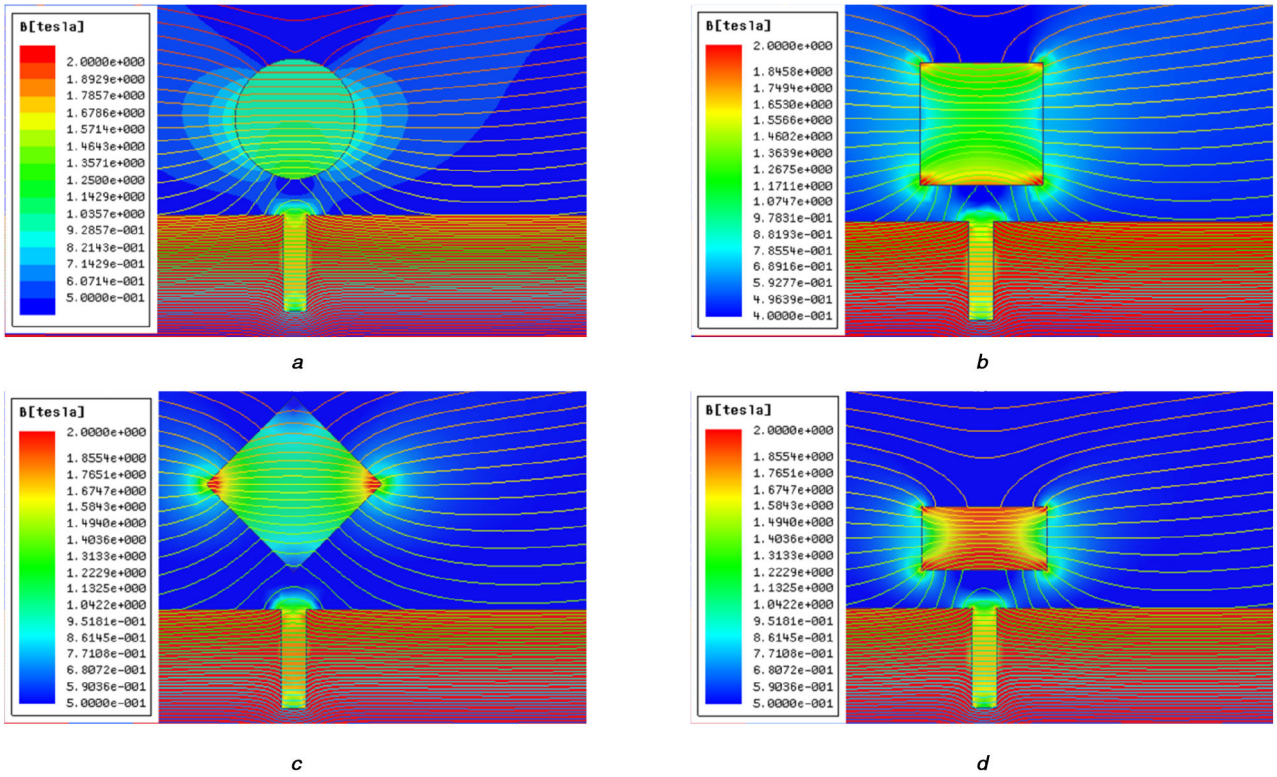

Fig. 3 *Distribution of the magnetic fields near a defect in the models with FMGs of various cross-sections*
(a) Round,
(b) Square,
(c) Diamond,
(d) Rectangle

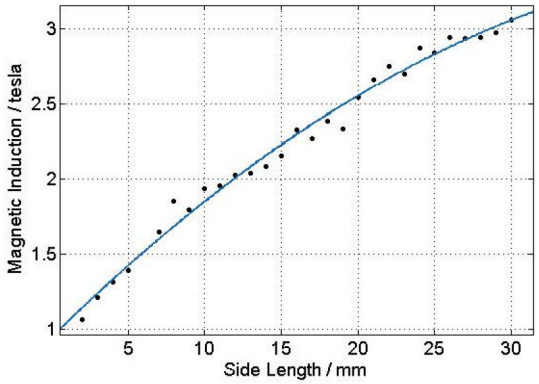

Fig. 4 *Relationship between the maximum magnetic induction and side length of a square cross-section*

3.2 Influence on the signal

Transient simulation is done with two FMGs of square and rectangular cross-sections. The relative speed of the FMG and the sample is 2 m/s. The location of the test points are shown in Fig. 5. The curves of the magnetic flux density at the test points are shown in Fig. 6. For a rectangular FMG, the density in the accumulation area is lower than that of a square FMG. It is also seen that the magnetic induction is stronger in the *Z*-direction.

As the side length of the FMG with a square cross-section increases, the magnetic flux density also increases. The relationship between the magnetic flux density peak and side length is shown in Fig. 7.

If no defect is in the surface of the sample, the LMF in the air is normally weak. The larger the lift-off, the weaker the output is. The magnetic flux density without a defect is represented by B_{back}. In actual detection, the sensor and yoke may vibrate and the lift-off is constantly changing. The sensor output and B_{back} vary as well [22]. It is difficult to differentiate the defect signals and vibration signals.

The peak-to-peak value of a defect signal is defined as B_{amp}. In further analysis, a coefficient α indicating the ratio of B_{am} to B_{back} is used

$$\alpha = \frac{B_{\text{amp}}}{B_{\text{back}}} \tag{6}$$

If B_{back} is large or B_{amp} is small, it is difficult to extract a defect signal from the background magnetic field. Hence, the signal is more likely disturbed with a lower α. The relationship between α and the side length is shown in Fig. 7.

From Fig. 7, it is seen that a larger side length of a cross-section contributes to easier detection of the MFL signal and easier disturbance. Hence, in the real tests, the size of the FMG should be chosen case by case. The two curves in the *X* and *Z* directions in Fig. 7 are intersected at a side length of 10 mm, which is treated as a suitable side length.

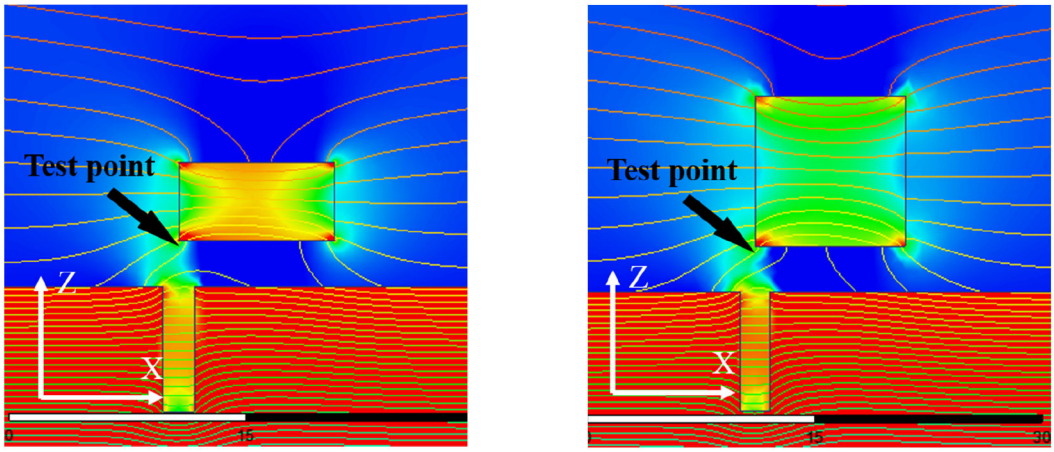

Fig. 5 *Position of the test points*
(a) Square cross-section,
(b) Rectangular cross-section

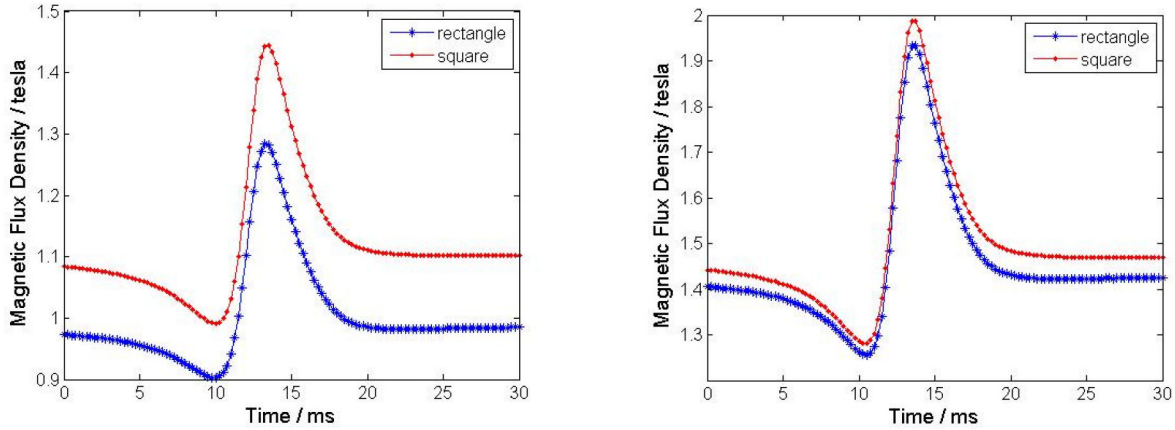

Fig. 6 *Variation of the magnetic flux density at the test points with respect to time*
(a) *X*-direction,
(b) *Z*-direction

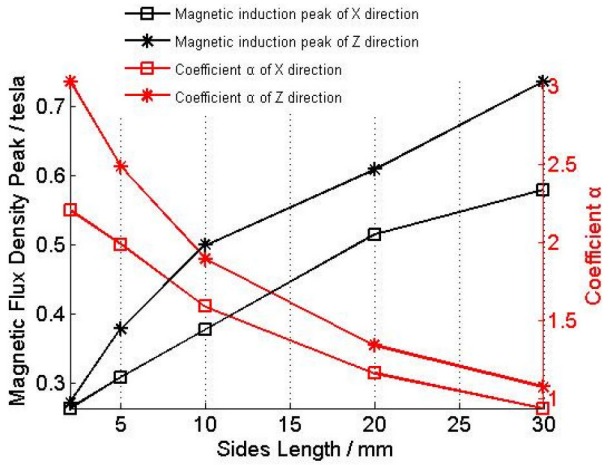

Fig. 7 *Relationship between α and the side length*

Table 2 Specifications of the hardware

Component	Model	Properties
sensor	UGN3503	output voltage of the Hall sensor is dozens of millivolts
amplifier	AD620	magnification is 100
DAQ card	ADLINK DAQ2208	sampling frequency is set to 10 kHz

4 Experimental study

4.1 Experimental system

For verification, an FMG-based MFL sensor was designed and a series of tests were carried out with an attempt to measure the *X* and *Z* components of the LMF. The detector consisted of an MFL probe, a set of signal conditioning and receiving circuit. The properties of the sensor, amplifier and data acquisition (DAQ) card are listed in Table 2. An AD620 instrumentation amplifier was used in a bias amplifier circuit. The scanning speed was 2 m/s and the sampling frequency was 10 kHz, which shall be sufficient for the experiment [17]. The block diagram of the test system is shown in Fig. 8*a*.

The outer casing of the probe was customised to detect small defects in the surface of the rail, as shown in Fig. 8*b*. Rubber wheels were mounted on both sides of the probe and the lift-off was 2–3 mm. The probe was internally mounted with a permanent magnet, a yoke, two Hall sensors and an FMG, which are shown in Fig. 8*c*. On the basis of the simulation results, a square cross-sectional FMG with a side length of 10 mm was made. The variation of the lift-off causes changes in the background magnetic field as well as interference to the sensor output. To eliminate the interference, a dual sensor for differential peak detection was used. When the probe vibrates, the outputs of the two sensors have almost the same amplitude and phase. When the probe detects a defect, the two sensors will receive signals with different phases, which are processed by subtraction. Thus, the interference caused by the vibration can be greatly eliminated. The subtraction in this

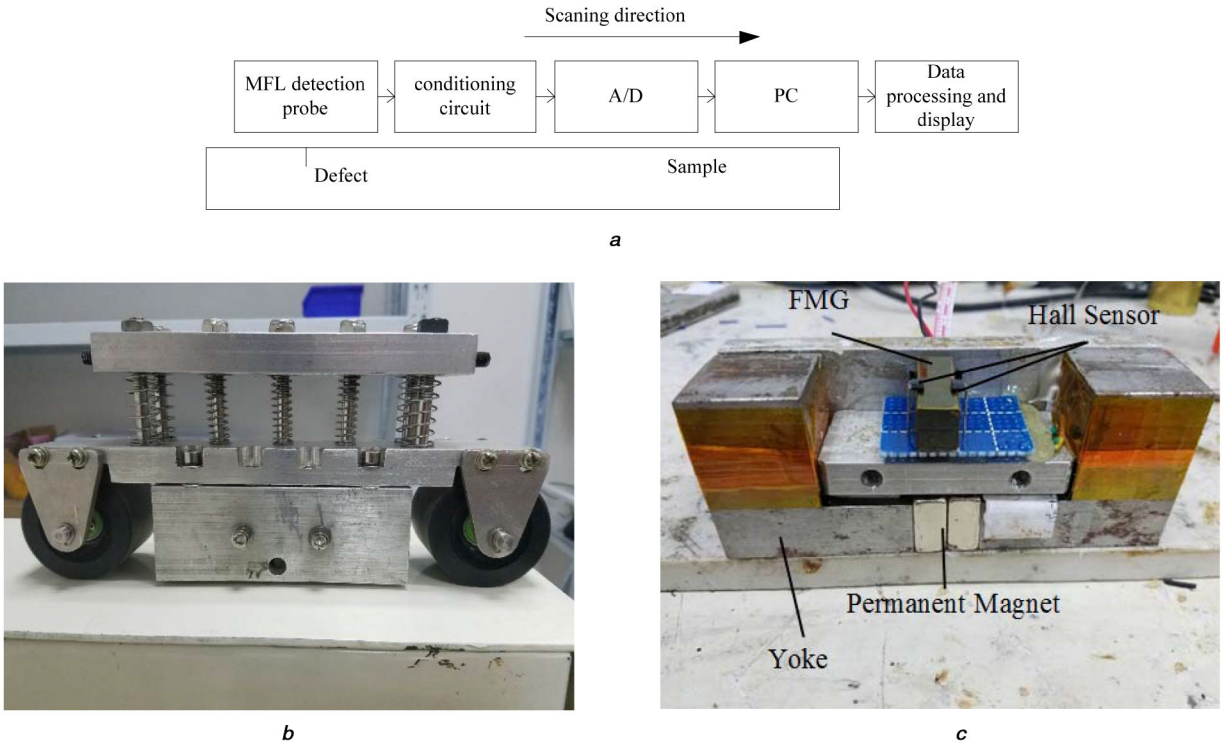

Fig. 8 *Test system*
(a) Block diagram,
(b) Outer casing,
(c) Internal structure

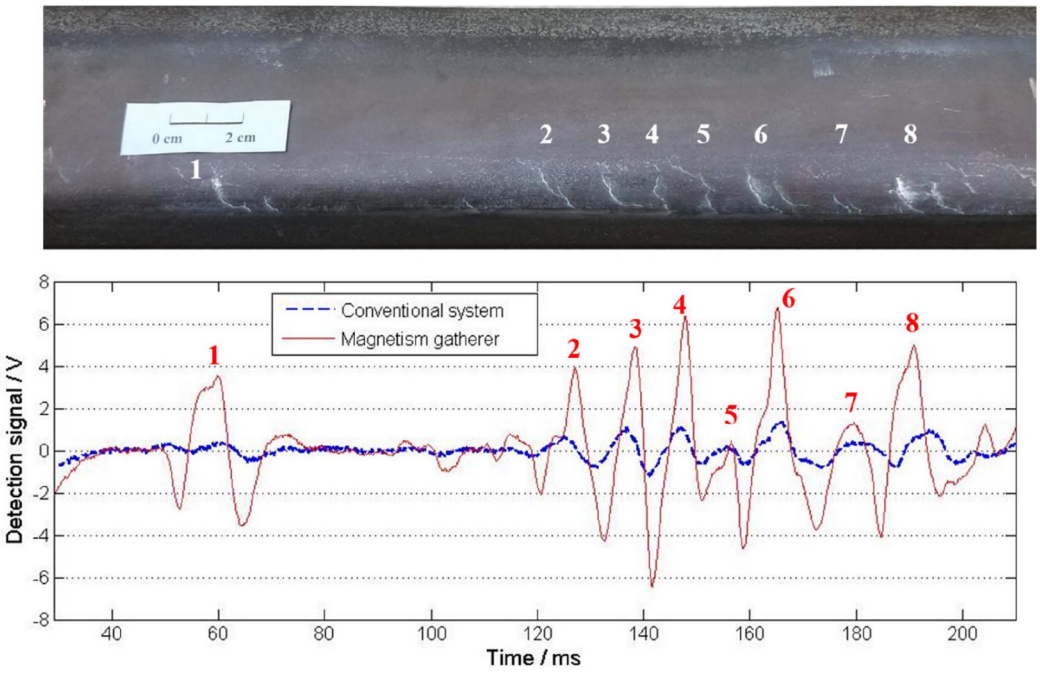

Fig. 9 *Comparison of test results of an FMG system and a conventional system for sample no. 1*

system is implemented by a hardware circuit, so it does not change the signal bandwidth of the detection system. This differential method was used in both conventional and FMG systems.

The rails used in the experiment had some small, dense natural defects, which were generally 0.03–0.15 mm deep and 0.05–0.20 mm wide.

4.2 Results and analysis

Figs. 9–12 shows the experimental results in the *Z*-direction of an FMG system and a conventional system. The probe was pushed by hand.

The detection signal from each defect is clearly observed. Since the width, depth and direction of defects are different, the detection signals of each defect are diverse. The signal amplitude of the FMG system is generally larger than that of the conventional system, and the dynamic range of the signal is also significantly increased. So the FMG system is better at detecting small defeats.

A stronger signal can result in a higher signal-to-noise ratio, which is advantageous for the detection of small defects. Natural defects are relatively short and narrow, so the corresponding MFLs are weak and difficult to detect by conventional system. Some natural defects are shown in Figs. 9–12. These defects are very difficult to detect by the conventional system, but can be detected

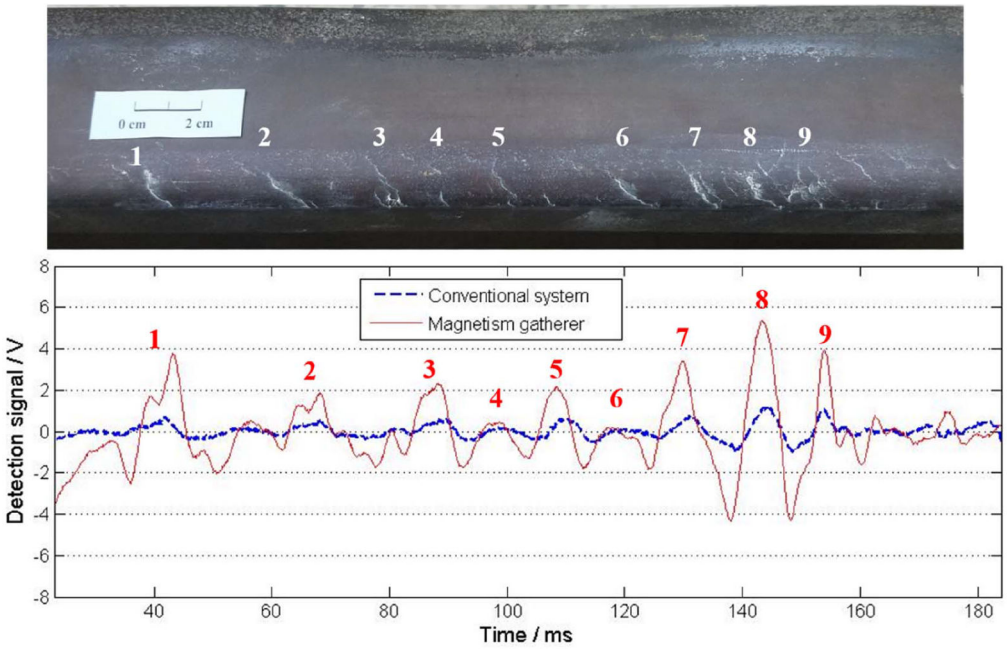

Fig. 10 *Comparison of test results of an FMG system and a conventional system for sample no. 2*

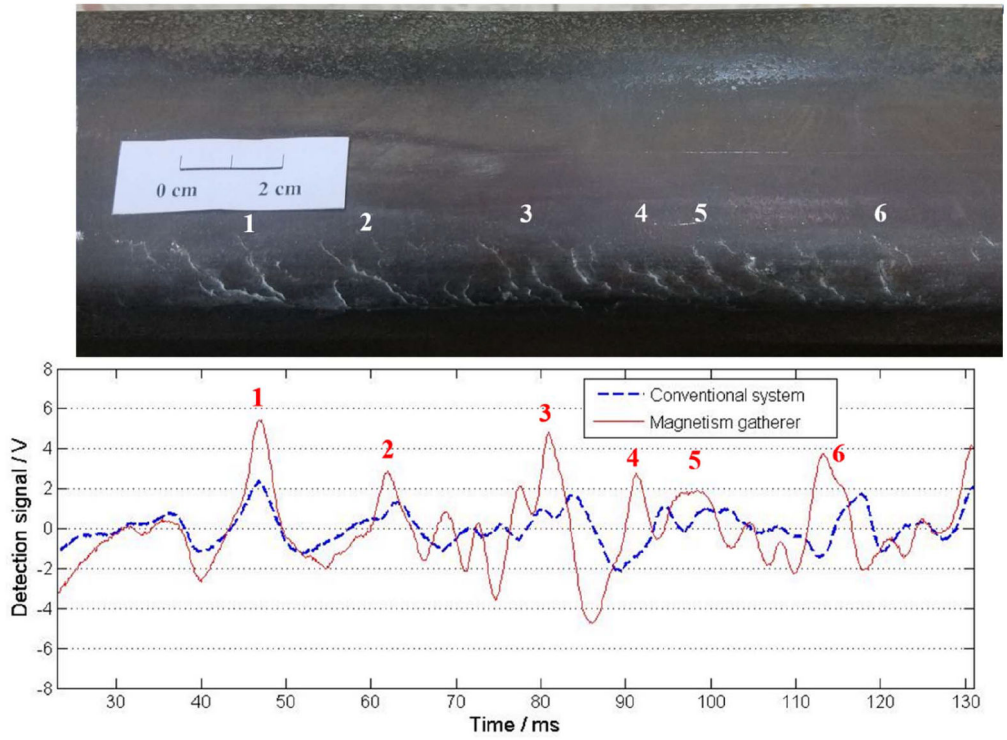

Fig. 11 *Comparison of test results of an FMG system and a conventional system for sample no. 3*

by the FMG system clearly. In Fig. 11, although the defects are very dense and the LMFs overlap with each other, more details are provided by the FMG system.

5 Conclusions

A new MFL detection method based on FMG has been presented. By adding an FMG near the sensor, the detection signal of a defect is amplified, and the MFL signal above the intact rail surface is also increased. To eliminate the unwanted interference, a differential detection method has been adopted. Natural defects have been detected by the system developed. Further study may be carried out to analyse the mechanism of interaction between the induced eddy current and FMG, and the magnetic gathering effect with a lift-off distance.

6 Acknowledgments

The work was financially supported by the Special Scientific Instrument Development of Ministry of Science and Technology of China (grant no. 2016YFF0103702) and the National Natural Science Foundation of China (grant no. 61527803).

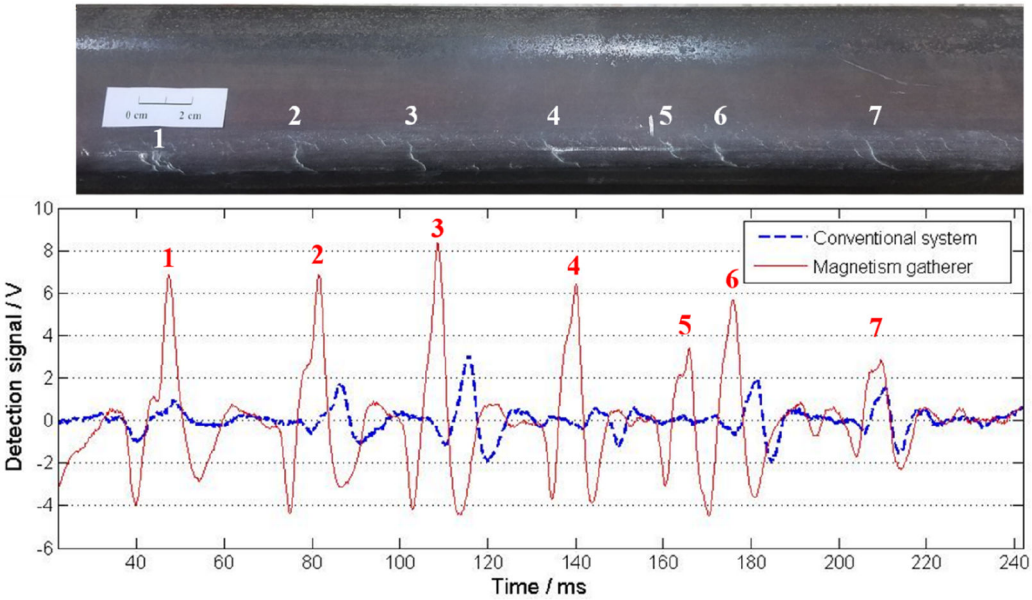

Fig. 12 *Comparison of test results of an FMG system and a conventional system for sample no. 4*

7 References

[1] Zhou, Q., Zhang, Y., Chen, C.: 'Issues about the steel rail for high-speed railway', *Railway Construct. Technol.*, 2004, **42**, (2), pp. 54–62

[2] Liu, Q., Zhang, B., Zhou, Z.: 'The research of wear characteristics on steel rail', *Mech. Eng. China*, 2002, **13**, (18), pp. 1596–1599

[3] Thomas, H., Heckel, T., Hanspach, G.: 'Advantage of a combined ultrasonic and eddy current examination for railway inspection trains', *Or Insight*, 2007, **49**, (6), pp. 341–344

[4] Pohl, R., Erhard, A., Montag, H.J., *et al.*: 'NDT techniques for railroad wheel and gauge corner inspection', *NDT E. Int.*, 2004, **37**, (2), pp. 89–94

[5] Gibert, X., Patel, V.M., Chellappa, R.: 'Robust fastener detection for autonomous visual railway track inspection'. IEEE Winter Conf. on Applications of Computer Vision, Hawaii, USA, 2015, pp. 694–701

[6] Guo-Hou, L.I., Huang, P.J., Chen, P.H., *et al.*: 'Application of eddy current testing in the quantitative evaluation of the rail cracks', *J. Zhejiang Univ.*, 2011, **45**, (11), pp. 2038–2042 o+ 2049

[7] Pohl, R., Krull, R., Meierhofer, R.: 'A new eddy current instrument in a grinding train'. Proc. of the ECNDT, Berlin, Germany, 2006, pp. 178–184

[8] Betz, C.E.: '*Principles of magnetic particle testing*' (Magnaflux Press, USA, 1967)

[9] Park, G.S., Park, E.S.: 'Improvement of the sensor system in magnetic flux leakage-type nondestructive testing (NDT)', *IEEE Trans. Magn.*, 2002, **38**, (2), pp. 1277–1280

[10] Wang, Z.D., Yao, K., Deng, B., *et al.*: 'Quantitative study of metal magnetic memory signal versus local stress concentration', *NDT E. Int.*, 2010, **43**, (6), pp. 513–518

[11] Sun, Y., Kang, Y.H.: 'Magnetic compression effect in present MFL testing sensor', *Sens. Actuators A, Phys.*, 2010, **160**, (1–2), pp. 54–59

[12] Wu, J., Fang, H., Huang, X., *et al.*: 'An online MFL sensing method for steel pipe based on the magnetic guiding effect', *Sensors*, 2017, **17**, (12), p. 2911

[13] Okolo, C.K., Meydan, T.: 'Pulsed magnetic flux leakage method for hairline crack detection and characterization', *AIP. Adv.*, 2017, **8**, (4), p. 047207

[14] Wu, J., Yang, Y., Li, E., *et al.*: 'A high-sensitivity MFL method for tiny cracks in bearing rings', *IEEE Trans. Magn.*, 2018, **54**, (6), pp. 1–8

[15] Tsukada, K., Majima, Y., Nakamura, Y., *et al.*: 'Detection of inner cracks in thick steel plates using unsaturated AC magnetic flux leakage testing with a magnetic resistance gradiometer', *IEEE Trans. Magn.*, 2017, **53**, (11), p. 1

[16] Wu, D., Liu, Z., Wang, X., *et al.*: 'Composite magnetic flux leakage detection method for pipelines using alternating magnetic-field excitation', *NDT E. Int.*, 2017, **91**, pp. 148–155

[17] Wang, P., Gao, Y., Tian, G.Y., *et al.*: 'Velocity effect analysis of dynamic magnetization in high-speed magnetic flux leakage inspection', *NDT E. Int.*, 2014, **64**, (2), pp. 7–12

[18] Han, W.H., Yuan, Y., Zhang, Y.X.: 'Research on finite element forward model for magnetic flux leakage testing of arbitrary shape defects', *Fire Control Command Control*, 2018, **43**, (1), pp. 80–84

[19] Li, E., Kang, Y., Tang, J., *et al.*: 'A new micro-magnetic bridge probe in magnetic flux leakage for detecting micro-cracks', *J. Nondestruct. Eval.*, 2018, **37**, (3), p. 46

[20] Bai, J., Wang, P., Zou, P.: 'A rail surface defect detection method based on the rail surface adaptive and bearing mechanism', *Nondestruct. Test.*, 2017, **39**, (11), pp. 16–19 o+ 30

[21] Sophian, A., Tian, G.Y., Zairi, S.: 'Pulsed magnetic flux leakage techniques for crack detection and characterisation', *Sens. Actuators A, Phys.*, 2005, **125**, (2), pp. 186–191

[22] Gao, Y.: 'Magnetic flux leakage technique for rail cracks online high-speed detection', Nanjing University of Aeronautics and Astronautics, 2013